Supplementary Materials

Collaborative Diagnostic Pathways for Unilateral Orbital Disease: A Clinicopathological Series

Supplementary Figure S1. Orbital Vascular Malformation (Cavernous Type): MRI

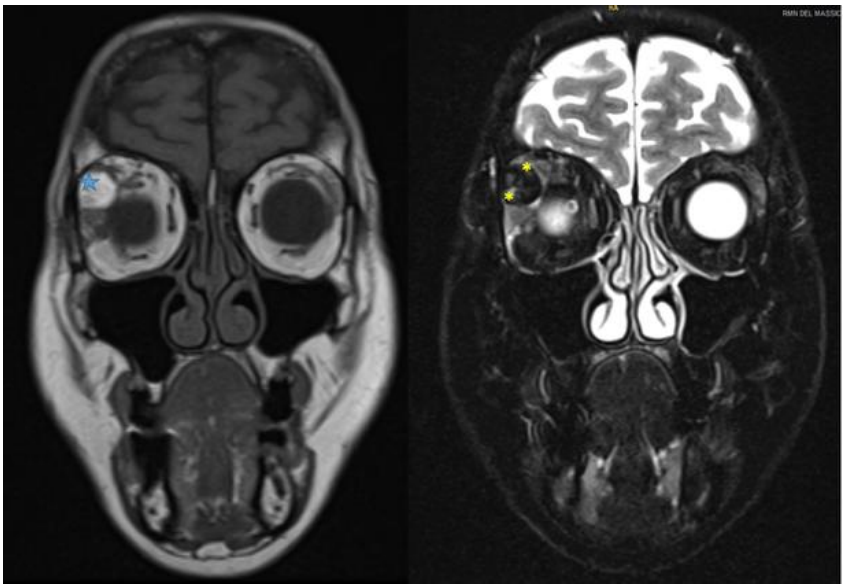

Figure S1A-B. *Axial T1 TSE (A) and axial T2 TSE Dixon fat-saturated (B) sequences. The right extraconal orbital lesion appears hyperintense on T1 (A, blue star) with signal dropout on fat-saturated T2 (B, yellow asterisks), consistent with a lipid-rich cavernous venous malformation compressing the medial rectus muscle.*

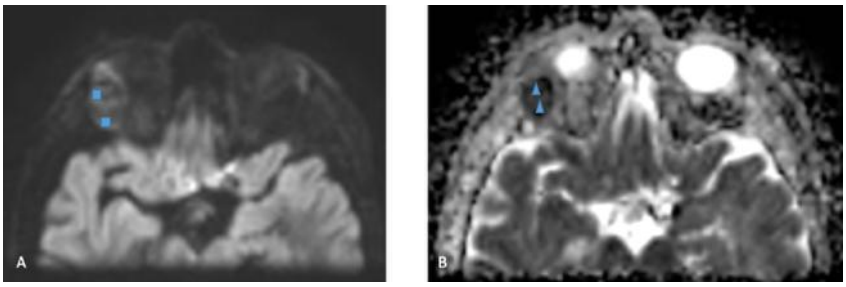

Figure S1C-D. *DWI at b = 800 s/mm2 (C) and ADC map (D) show no restricted diffusion, confirming the non-proliferative, low-flow nature of the lesion.*

Supplementary Figure S2. Orbital Vascular Malformation: Clinical Presentation

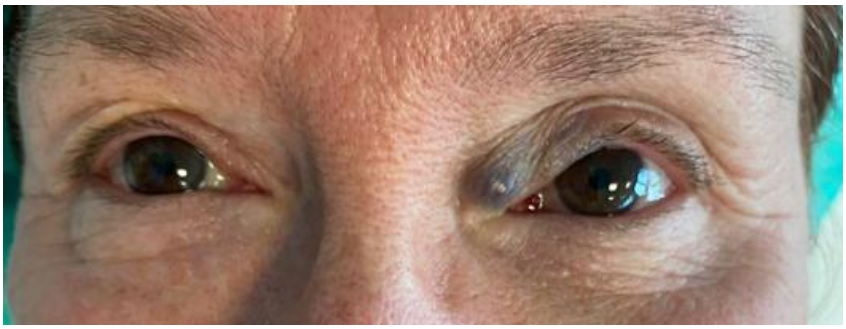

Figure S2. *Clinical photograph demonstrating unilateral right medial canthal swelling with associated pseudoptosis. The lesion was soft, bluish, and compressible on palpation, characteristic features of a superficial venous malformation.*

Supplementary Figure S3. Chronic Idiopathic Orbital Inflammation: Intraoperative Findings, Histopathology, and MRI

Figure S3A. *Intraoperative photograph showing the nodular orbital mass (greatest dimension 2.3 cm) during anterior orbitotomy, performed concurrently with upper eyelid blepharoplasty.*

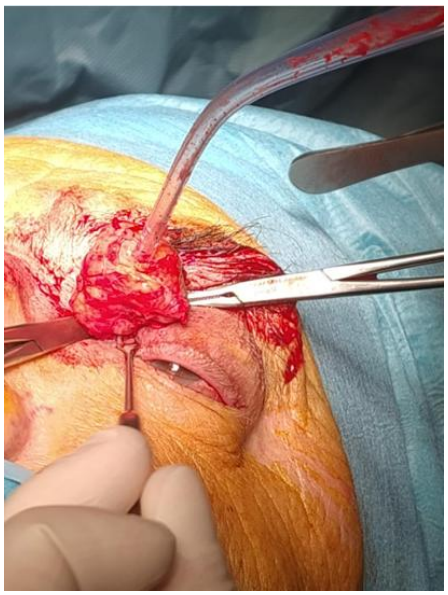

Figure S3B. *Intraoperative photograph showing incisional biopsy of the orbital mass. The lesion appeared grayish with a smooth surface and a compact, yellowish-white, homogeneous cut section.*

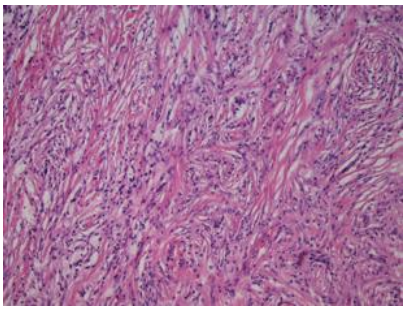

Figure S3C. *H&E (20x): Spindle cell proliferation with wavy, interlacing fascicles embedded in dense sclerohyaline stroma, with scattered small lymphocytes. No cytological atypia, mitotic figures, or necrosis.*

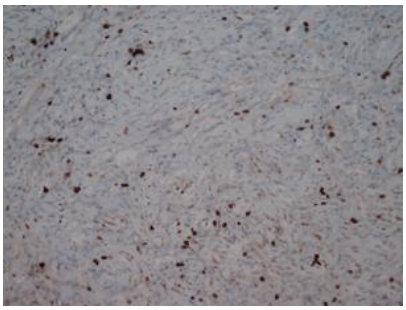

Figure S3D. *Ki-67 immunohistochemistry: Sparse nuclear positivity confirming a low proliferative index (<5%), consistent with a non-neoplastic fibroinflammatory process.*

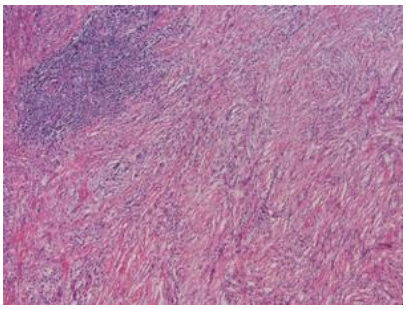

Figure S3E. *H&E (10x): Lower-magnification view showing the fibrosclerotic spindle cell stroma with a prominent reactive lymphoid aggregate, representing the mixed inflammatory component.*

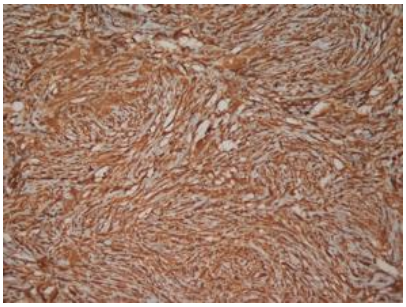

Figure S3F. *Vimentin immunohistochemistry: Diffuse cytoplasmic positivity in spindle cells. All other markers (ALK, actin ML, CD3, CD14, CD20, CD21, CD23, CD34, CD163, CK AE1/AE3, desmin, ERG, fascin, HHV8, SOX10, STAT6, S100) were negative.*

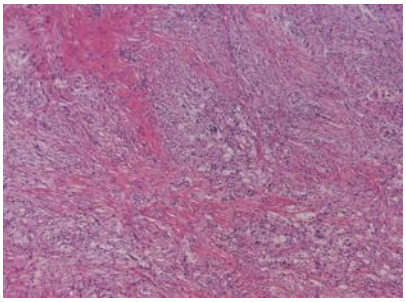

Figure S3G. *H&E (10x): Additional field illustrating the mixed lymphohistiocytic infiltrate within the fibrosclerotic stroma. Immunostaining (not shown) confirmed CD3+, CD20+, and CD163+ populations, excluding lymphoma and IgG4-related disease.*

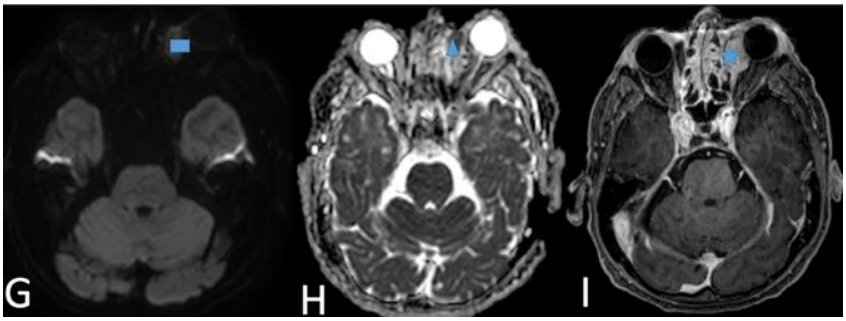

Figure S3H-J. *MRI of chronic fibrosing IOI. DWI at b = 1000 s/mm2 (H) shows a hyperintense inferomedial orbital mass. The ADC map (I) confirms restricted diffusion (ADC <1.0 x 10-3 mm2/s). Gadolinium-enhanced 3D T1 VIBE with fat suppression (J) demonstrates avid contrast enhancement, consistent with active fibrosing inflammation.*

Supplementary Figure S4. Acute Idiopathic Orbital Inflammation: MRI and Clinical Presentation

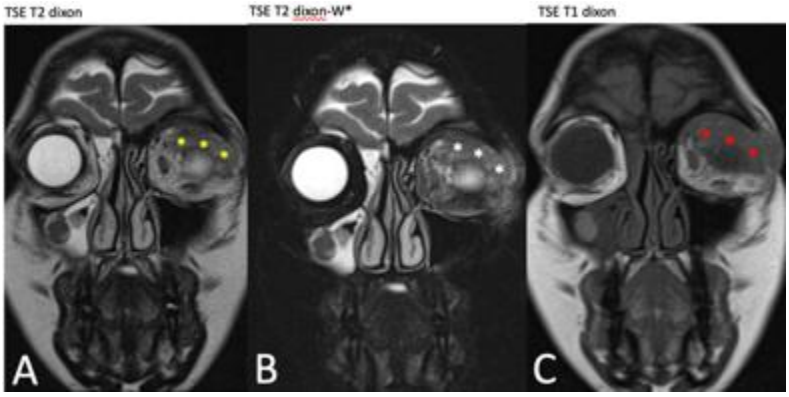

Figure S4A-C. *Axial T2 TSE Dixon (A), T2 TSE Dixon fat-saturated (B), and T1 TSE Dixon (C) sequences demonstrate hypointense signal in the left orbital fat and thickening of the superior and lateral rectus muscles, consistent with diffuse acute orbital inflammation without bone erosion.*

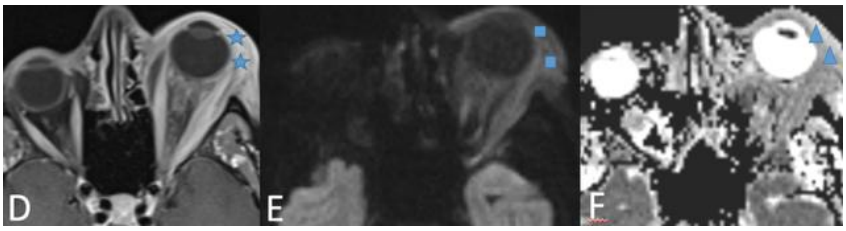

Figure S4D-F. *Gadolinium-enhanced 3D T1 VIBE (D, blue stars) shows contrast enhancement of the left lateral rectus muscle and upper eyelid. DWI at b = 1000 s/mm2 (E) and ADC map (F, arrowheads) demonstrate no diffusion restriction with elevated ADC values, distinguishing acute inflammatory disease from lymphoproliferative or neoplastic infiltration.*

Figure S4G. *Close-up photograph of the left eye demonstrating severe conjunctival chemosis, marked hyperemia, and dilated episcleral vessels in a caput medusae pattern, with air visible in the subconjunctival space. The cornea was clear.*

Figure S4H. *Frontal clinical photograph showing complete left upper eyelid ptosis with massive periorbital swelling and proptosis (32 mm Hertel). Exohypotropia and diplopia in all gaze positions were present. Pupils were isocoric and normally reactive.*

Figure S4I. *Clinical photograph following multiple endorbital biopsies of the left orbit, supero-lateral external orbital decompression, and functional endoscopic sinus surgery (FESS). Periorbital swelling is markedly reduced compared to the preoperative state.*

Supplementary Figure S5. Spheno-Orbital Meningioma: CT Imaging

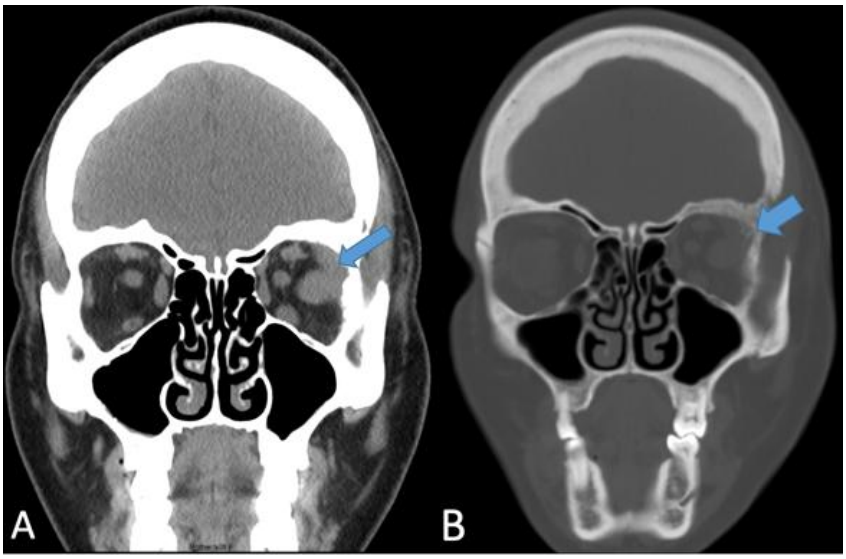

Figure S5A-B. *Coronal non-contrast CT. Soft tissue window (A) shows thickening of the extraconal adipose tissue adjacent to the left lateral rectus muscle (arrow). Bone window (B) demonstrates associated osteolytic and osteosclerotic remodelling of the frontal bone (arrow), characteristic of spheno-orbital meningioma with osseous involvement.*

Supplementary Figure S6. Solitary Orbital Neurofibroma: Clinical Presentation, MRI, and Histopathology

Figure S6A. *Preoperative clinical photograph demonstrating right upper eyelid mechanical ptosis with superomedial orbital fullness. The mass was firm, non-pulsatile, and non-tender, without signs of inflammation or stigmata of neurofibromatosis type 1.*

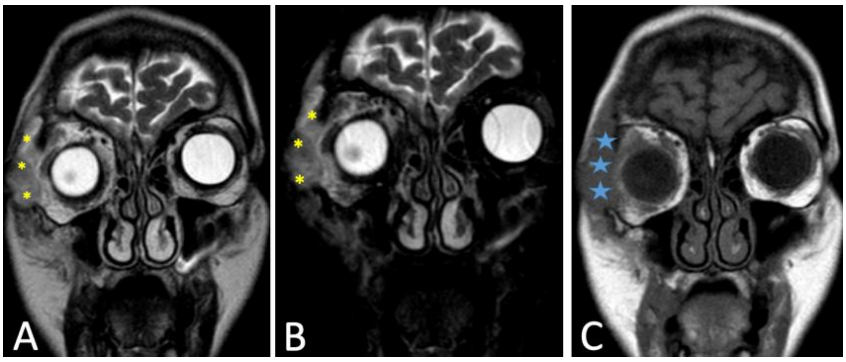

Figure S6B-D. *Coronal T2 TSE (B, yellow asterisks), T2 fat-saturated (C, yellow asterisks), and T1 TSE (D, blue stars) sequences demonstrate a solid, hypointense lesion in the right lateral orbital region involving the subcutaneous tissue and lateral orbital wall. No intracranial extension is identified.*

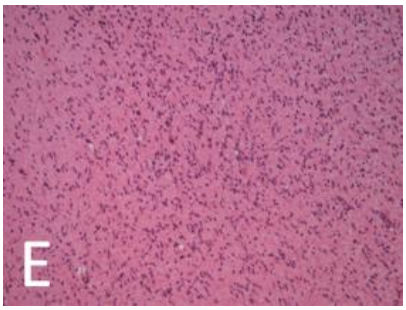

Figure S6E. *H&E (E): Diffuse growth pattern of the neurofibroma, with loosely arranged oval to spindle cells in a pale myxoid stroma, representing a mixture of Schwann cells and perineural fibroblasts. No atypia or mitotic activity.*

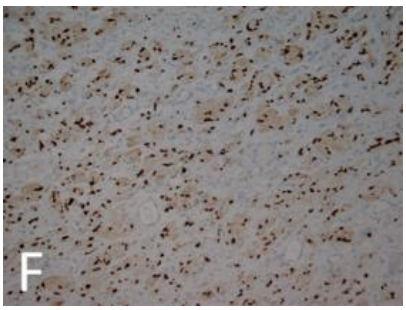

Figure S6F. *SOX10 immunohistochemistry (F): Diffuse nuclear positivity confirming Schwann cell differentiation. Ki-67 proliferative index was below 1%.*

Supplementary Figure S7. Lacrimal Gland Adenoid Cystic Carcinoma: Exenteration Specimen and Histopathology

Figure S7A. *Orbital exenteration specimen including the globe and surrounding orbital soft tissues en bloc. A surgical ruler indicates the dimensions of the resected specimen.*

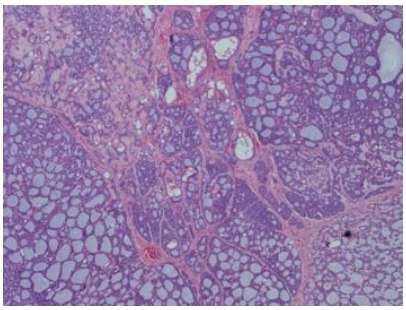

Figure S7B. *H&E (4x): Large basaloid epithelial nests with a predominant cribriform architecture. Pseudocystic spaces are filled with basophilic amorphous material and separated by fibrovascular septa, characteristic of adenoid cystic carcinoma.*

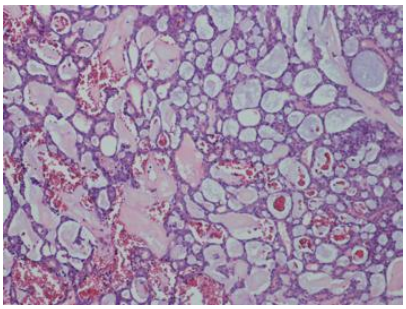

Figure S7C. *H&E (10x): Cribriform nests of atypical basaloid cells with round pseudocystic spaces at intermediate magnification. Associated stromal haemorrhage is present.*

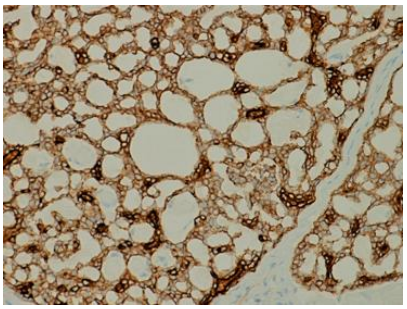

Figure S7D. *Pan-cytokeratin (CK pool) immunohistochemistry: Membranous and cytoplasmic positivity delineating the neoplastic epithelial cells within the cribriform nests, confirming the glandular epithelial origin of the tumour.*

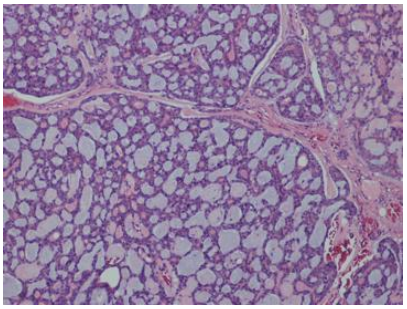

Figure S7E. *H&E (10x): Perineural infiltration with tumour nests immediately adjacent to and encircling a nerve fascicle (central fibrous structure). Perineural invasion is a key prognostic factor associated with local recurrence in lacrimal gland ACC.*

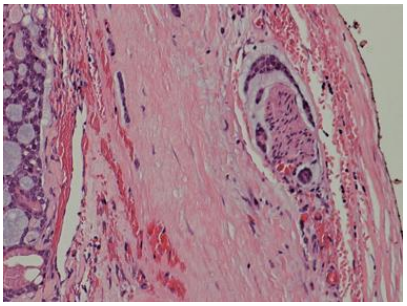

Figure S7F. *H&E (20x): High-magnification view of perineural invasion, with tumour cells tightly encircling a nerve fascicle showing a well-defined perineurium. This finding is associated with reduced disease-specific survival and guides the extent of surgical resection.*

Supplementary Figure S8. Lacrimal Gland ACC: Clinical Presentation, Surgical Findings, and Postoperative Outcome

Figure S8A. *Preoperative clinical photograph demonstrating right superolateral orbital swelling and upper eyelid fullness with mild globe displacement, consistent with a lacrimal gland mass.*

Figure S8B. *Intraoperative photograph following right orbital exenteration with resection of the lateral orbital wall, part of the orbital roof, and the zygomatic arch. The orbital cavity is shown after removal of all orbital contents.*

Figure S8C. *Early postoperative photograph after orbital exenteration and craniofacial reconstruction. The exenterated right orbital socket is closed; a surgical drain is visible at the oral commissure. The forehead incision reflects the craniofacial surgical approach.*

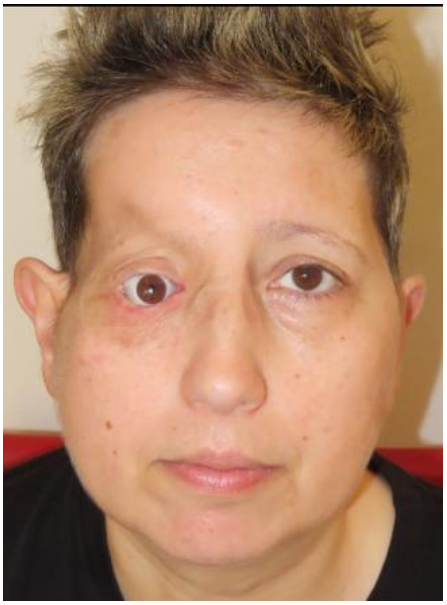

Figure S8D. *Postoperative clinical photograph at follow-up demonstrating satisfactory craniofacial reconstruction after right orbital exenteration. No gross residual tumour is present in the orbital cavity and no intracranial disease extension was identified on imaging.*

Supplementary Figure S9. Lacrimal Gland ACC: MRI Findings

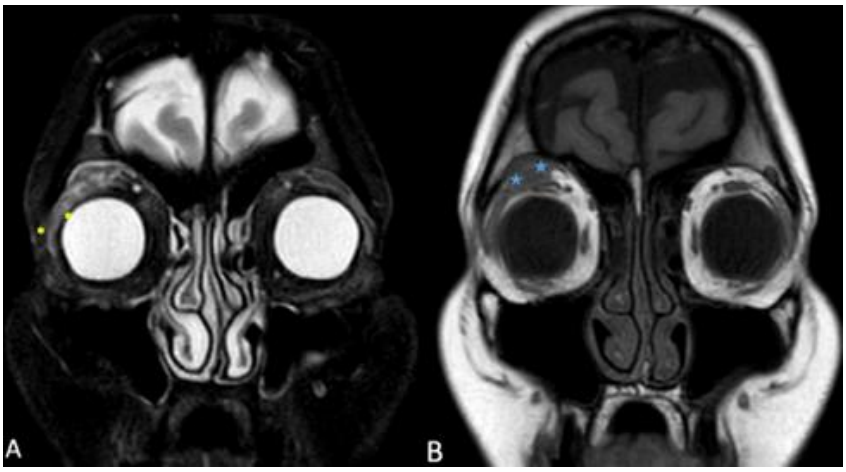

Figure S9A-B. *Axial T2 TSE Dixon (A, yellow dots) and coronal T1 TSE (B, blue stars) sequences demonstrate a T1-hypointense lesion in the right superolateral extraconal fat adjacent to the superior rectus, corresponding to the lacrimal gland ACC primary site.*

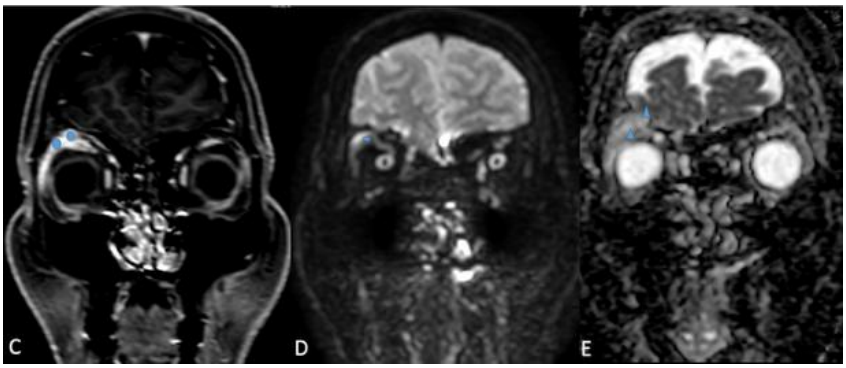

Figure S9C-E. *Gadolinium-enhanced T1 fat-saturated coronal (C, blue dot) shows contrast enhancement of the right lacrimal gland region. DWI coronal (D) demonstrates restricted diffusion of the lesion. T2 fat-saturated coronal (E, arrowheads) confirms T2 hyperintensity of the right superolateral extraconal mass.*

Supplementary Figure S10. Basal/Basosquamous Cell Carcinoma with Orbital Extension: Clinical Presentation and Surgery

Figure S10A. *Clinical photographs of a patient with right periocular basosquamous carcinoma before immunotherapy. Frontal (top) and oblique (bottom) views show involvement of the medial canthus and lower eyelid with periorbital swelling, limitation of downgaze, and presumed periosteal infiltration.*

Figure S10B. *Clinical photograph at disease progression after immunotherapy, showing a deeply ulcerated and necrotic periocular lesion with destruction of the medial canthal region and orbital extension. Orbital exenteration was subsequently performed.*

Figure S10C. *Clinical photograph of a second patient with recurrent invasive basal cell carcinoma of the right lateral periocular region, with extension to the cheek. Prior surgical scarring is present.*

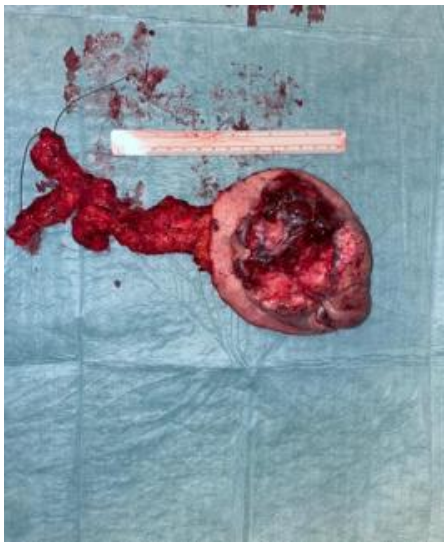

Figure S10D. *Orbital exenteration specimen including the globe, orbital contents, and involved periorbital soft tissues en bloc, with the attached optic nerve and orbital fat. A surgical ruler indicates specimen dimensions.*

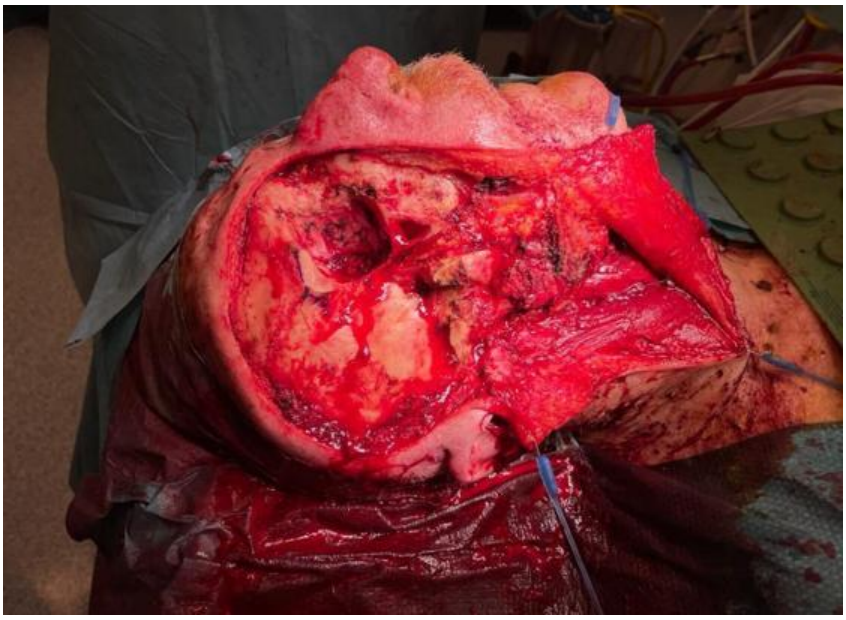

Figure S10E. *Intraoperative photograph showing the surgical field after extended orbital exenteration with craniofacial resection, including removal of the lateral orbital wall and adjacent bone.*

Figure S10F. *Intraoperative photograph showing inset of a pedicled myocutaneous flap for reconstruction of the orbital and craniofacial defect following extended exenteration.*

Supplementary Figure S11. Squamous Cell Carcinoma with Orbital Involvement: Clinical Presentation and Surgery

Figure S11A. *Clinical photograph of an advanced ulcerated and indurated periocular squamous cell carcinoma with abundant keratin formation, causing near-complete palpebral occlusion and massive local destruction of the eyelid and periorbital tissues.*

Figure S11B. *Intraoperative photograph following orbital exenteration, showing closure of the orbital defect with mattress sutures.*

Supplementary Figure S12. Primary Mucinous Carcinoma of the Eyelid: Clinical Presentation

Figure S12. *Clinical photograph showing a translucent, glistening lesion along the lower eyelid margin with a gelatinous surface and telangiectatic vessels, extending toward the medial canthus. This mucin-rich appearance is characteristic of primary mucinous carcinoma of the eyelid.*

Supplementary Figure S13. Merkel Cell Carcinoma: Clinical Presentation

Figure S13. *Clinical photographs showing a rapidly growing red-violaceous nodule at the right medial canthal region, extending beneath the upper and lower eyelids. The vascular surface, violaceous hue, and rapid growth are characteristic features of Merkel cell carcinoma. Regional nodal disease was confirmed at staging.*